

Sun-Heliosphere Observation-based Ionization Rates Model

Justyna M. Sokół^{1,*}, D. J. McComas¹, M. Bzowski², M. Tokumaru³

¹Department of Astrophysical Sciences, Princeton University, Princeton, NJ, USA
(jsokol@princeton.edu, jsokol@helio.zone)

* NAWA Bekker Fellow

²Space Research Centre, PAS (CBK PAN), Warsaw, Poland

³Institute for Space-Earth Environmental Research, Nagoya University, Nagoya, Japan

ABSTRACT

The solar wind (SW) and the extreme ultraviolet (EUV) radiation modulate fluxes of interstellar and heliospheric particles inside the heliosphere both in time and in space. Understanding this modulation is necessary to correctly interpret measurements of interstellar neutral gas, energetic neutral atoms, pickup ions, and helioglow radiation measured inside the heliosphere. We report a change of heliospheric ionization rates due to the update of the SW and solar EUV data, revise the calculation of these ionization rates, and provide the most up-to-date version of the model of the Sun-Heliosphere Observation-based Ionization Rates (SHOIR). With the new results, we study the in-ecliptic variation of the SW parameters, the latitudinal structure of the SW speed and density, and the reconstruction of the photoionization rates based on the currently available data. We observe a significant change in the total ionization rates for O and Ne (up to 30%) and the latitudinal variations of the total ionization rates for H (up to 50%). The new rates are higher than previously thought. The least affected are the ionization rates for He, being about 10%. The changes are the greatest for the solar maximum period of the solar cycle 24. We discuss the consequences of the update of the ionization rates for the study of the heliosphere.

1. INTRODUCTION

The Sun influences the interstellar medium and the interstellar particles inside the heliosphere through the ionization processes. The primary interaction is the resonant charge exchange with the solar wind (SW) protons, and the other is photoionization by the solar extreme ultraviolet (EUV) radiation and impact ionization by the SW electrons (e.g., Blum & Fahr 1970, Thomas 1978, Ruciński & Fahr 1989). The distribution of active regions and coronal holes on the Sun varies in time, modulating the solar EUV flux and SW. During solar minimum, the SW is fast at high latitudes emerging from expanded polar coronal holes and slow and dense in the equatorial band (e.g., McComas et al. 1998, 2000). As the solar activity increases, the slow and dense SW from the equatorial band and fast wind from the polar coronal hole both spread and are present at all latitudes. The SW varies on shorter and longer time scales; however, the quasi-periodic solar cycle (SC) variations of the SW speed and density present out of the ecliptic plane, are not observed in the ecliptic plane. The solar EUV flux and the solar EUV proxy time series (Dudok de Wit 2011, Dudok de Wit & Bruinsma 2011) measured in the ecliptic plane vary with the SC. The flux is higher during solar maximum and smaller during solar minimum. Also, the

latitudinal variations of the solar EUV flux are observed (Cook et al. 1980, Cook et al. 1981a, Pryor et al. 1992, Auchère et al. 2005a, 2005b).

The temporal and spatial variations of the solar output vary the EUV- and SW-driven ionizing environment inside the heliosphere and modulate the ISN gas which enters the heliosphere from the Very Local Interstellar Medium (VLISM) and the fluxes of its derivative particles: pickup ions (PUIs) and energetic neutral atoms (ENAs) (e.g., Sokół 2016), as well as the heliospheric backscatter glow (Bzowski et al. 2002, 2003). This modulation needs to be accounted for to correctly assess the attenuation of the flux of particles traveling from the edges of the heliosphere to detectors in the vicinity of the Earth's orbit and to interpret the measurements to study of the process at the boundary regions of the heliosphere, like, e.g., the *Interstellar Boundary Explorer* (IBEX; McComas et al. (2009)) observations. IBEX has been measuring the ISN gas of H, He, Ne, O, and D as well as the H ENAs starting at the end of 2008. Moreover, this period coincides with the SC 24, which began in December 2008 and lasted probably to April 2019,

when the first sunspots indicating the new SC 25, was recorded¹.

Most of the in-situ measurements of the SW, ISN gas, ENAs, and PUIs are collected by instruments in the ecliptic plane. However, the measured particles pass various latitudes, especially when detected in the downwind hemisphere. In consequence, the latitudinal variations of the ionization rates reflect in the data, as pointed out, for example, for ISN O and O⁺ PUI densities by Sokół et al. (2019b). Ruciński et al. (1996) studied the ionization processes for the interstellar neutral (ISN) gas species and methods for their determination inside the heliosphere. Sokół et al. (2019a) studied the fractional contribution of different ionization processes to the total ionization rates for various species, their variation in time, and as a function of heliographic latitude². These authors used the SW variations over time as a function of latitude after Sokół et al. (2013) for the SW speed, and Sokół et al. (2015) and McComas et al. (2014, Appendix B) for the SW density, and calculated the charge exchange and electron impact ionization reactions. They calculated the latter reaction following the methodology proposed by Ruciński & Fahr (1989, 1991), which was next developed by Bzowski (2008) based on measurements of electron temperature by *Helios* inside 1 au and *Ulysses* inside 5 au. Sokół et al. (2019a) calculated the photoionization rates using a multi-component model based on EUV spectral data and the solar EUV proxy data (Bzowski et al. 2013a,b; Bochsler et al. 2014). However, the multi-component model for photoionization rates is sensitive to calibration issues of the component data, as discussed by, e.g., Sokół & Bzowski (2014).

The SW and solar EUV data, which are commonly used to calculate the ionization rates, underwent a series of revisions and new releases in SC 24. The changes are due to various reasons, but collectively they influence estimation of the ionization rates inside the heliosphere. In this paper, we focus on changes in the SW and solar EUV data that happened during the period of *IBEX* observations. We concentrate on the consequences for the assessment of

the heliospheric ionization rates following the available methodology. Firstly, we discuss the in-ecliptic SW (Section 2) and the latitudinal structure of the SW (Section 3). Then, we present an upgrade of the photoionization rates (Section 4). We present the final model in Section 5. In Section 6, we discuss the implications of the update of the data used to calculate the ionization rates for the study of the heliosphere.

2. IN-ECLIPTIC SOLAR WIND

The in-ecliptic SW has been measured since the 1960s by instruments on various missions. The data are collected and inter-calibrated in the OMNI database (King & Papitashvili 2005). This database underwent a few data release changes in recent years related to data cross-normalization (e.g., February 2013, April 2019³). The changes concerned data mostly from 1995 onward. For the time series averaged over Carrington rotation (CR), which is a present baseline time resolution in the study of heliospheric ionization rates (Bzowski 2008, Bzowski et al. 2013a,b), the changes are from less than 1%, in case of the SW speed, and up to 30% for SW density and n_{α}/n_p . In the present study, we use SW speed, density, and n_{α}/n_p from the OMNI most current data released in April 2019. Although the OMNI database description⁴, provides some uncertainty estimates, the hourly time series we use does not contain information about the data accuracy of individual records, and thus, we do not refer to the data accuracy in this paper.

The in-ecliptic SW parameters at 1 au averaged over CR for the last three SCs are presented in Figure 1. We calculate the CR averages from the hourly data, and we assess the data variability calculating the mean standard deviation of the hourly SW data, which is 87 km s⁻¹ for speed, 5 cm⁻³ for density, and 0.02 for n_{α}/n_p . The SW speed and density do not vary periodically with the solar activity, in contrast to n_{α}/n_p , which variations follow the SC. For a guidance of the SC-variations, we present the sunspot number (SSN⁵), a standard proxy for determination of the solar activity level, in the top panel of Figure 1. The in-ecliptic SW varies mostly on smaller or longer

¹Source:

http://sprg.ssl.berkeley.edu/~tohban/wiki/index.php/A_Sunspot_from_Cycle_25_for_sure

2. We use heliolatitude interchangeably to heliographic latitude later in the text.

³Source:

https://omniweb.gsfc.nasa.gov/html/ow_news.html

⁴ https://omniweb.gsfc.nasa.gov/html/ow_data.html

⁵ Source: WDC-SILSO, Royal Observatory of Belgium, Brussels

time scales, which are related to the presence of coronal holes and active regions or long-term changes. The net SW density decreased almost step-like from $\sim 8.3 \text{ cm}^{-3}$, in the period from 1985 to 1998 to about $\sim 5.7 \text{ cm}^{-3}$, in the period from 1998 to 2014 (see, e.g., McComas et al. 2008, Sokół et al. 2013). Next, the SW density increased to $\sim 6.6 \text{ cm}^{-3}$ in 2014 and remains like this up to the present.

The decrease of the SW density affected the SW dynamic pressure⁶, which is an essential factor in the study of the heliosphere, its dimensions, and processes in the heliosheath (McComas et al. 2017, 2018, 2019; Zirnstein et al. 2018). The declining trend for the SW dynamic pressure was observed starting from the intensification in ~ 1991 and continued to 2014 when it rapidly increased, followed by a gradual and slow decrease after 2015 (see Figure 1). Interestingly, during the overall decrease, an intensification of the SW dynamic pressure happened also in 2003/2004.

The n_α/n_p is the in-ecliptic SW parameter, which clearly varies quasi-periodically with the solar activity at 1 au. The variations are from 0.01 to 0.07 and correlate with the SW speed (Kasper et al. 2007, Alterman & Kasper 2019). The overall, long-term decrease of the n_α/n_p is also observed; the maximum n_α/n_p was 0.085 in SC 22, 0.062 in SC 23, and 0.050 in SC 24, while the minimum changed from 0.017 to 0.011 from SC 22 to SC 24. The n_α/n_p is a parameter in the calculation of the charge exchange reaction with alpha particles for He atoms (Bzowski et al. 2012), the electron impact ionization, the SW energy flux, and the SW dynamic pressure. In the present study, we use the measured variations of the n_α/n_p in time in the ecliptic plane.

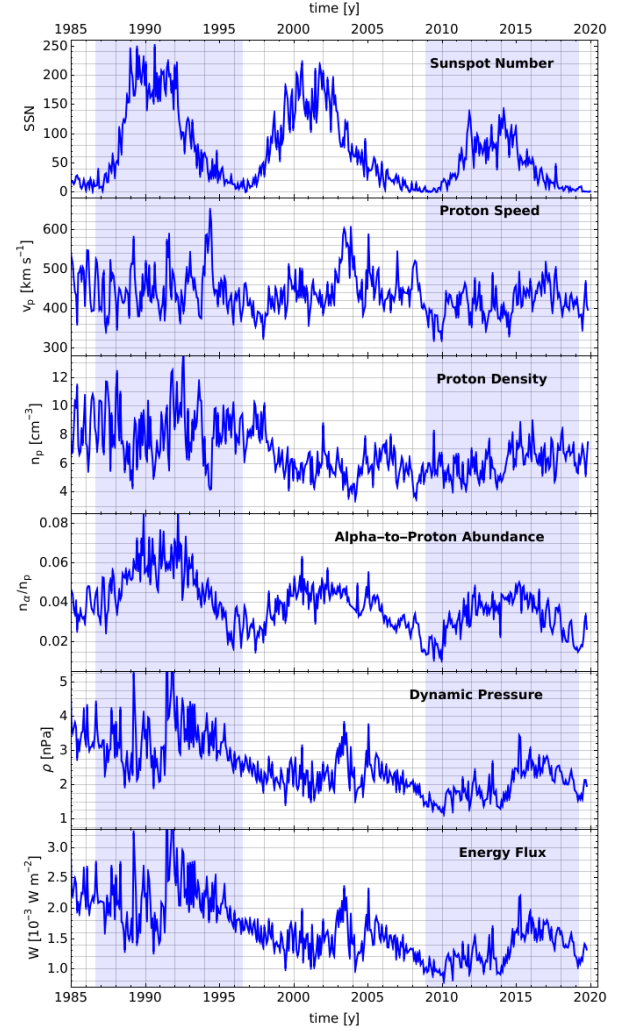


Figure 1: From top to bottom: SSN, SW proton speed, density, alpha-to-proton abundance, dynamic pressure, and energy flux in the ecliptic plane at 1 au, CR-averaged in time. The blue shaded regions encompass the SC 22 and SC 24.

3. SOLAR WIND LATITUDINAL STRUCTURE

The latitudinal variation of the SW flow was observed by the remote study of the SW by interplanetary scintillations (IPS; Dennison & Hewish 1967, Kakinuma 1977, Coles et al. 1980) and by in-situ measurements by *Ulysses* (McComas et al. 1998, 2000). *Ulysses* measured SW out of the ecliptic plane from 1992 to 2009, providing reference data for the SW latitudinal structure. After termination of the *Ulysses* mission, the SW latitudinal structure is only

⁶ $\rho_{\text{SW}} = n_p v_p^2 (m_p + n_\alpha/n_p m_\alpha)$, where n_p - SW proton density, v_p - SW proton speed, m_p - proton mass, m_α - alpha particle mass, n_α/n_p - alpha-to-proton number abundance

studied indirectly. The ground-based IPS observations, like, e.g., those conducted regularly from 1985 onward by the Institute for Space-Earth Environmental Research (ISEE) at Nagoya University (Tokumaru et al. 2010, 2012) are one of the methods to study of the SW remotely.

The multi-antenna system to observe IPS provided by ISEE allows estimating the SW speed as a function of latitude based on a study of a delay time of the measured scintillation pattern of the radio signal between the stations. This IPS observation facility was upgraded with a higher efficiency antenna in Toyokawa in 2010 (Tokumaru et al. 2011), which allows for an increase of sensitivity of the system and thus an increase in the number of observed radio sources while reducing the number of line-of-sight. After the break in the operation in 2010 due to the system upgrade, the regular IPS observations of the SW speed recovered in 2011. However, the IPS-derived SW speed began to diverge from the in-ecliptic measurement data collected by OMNI. The difference increased in time and was greater than 100 km s^{-1} , during the solar maximum of SC 24 (see Figure 2, also Sokół et al. (2017)).

In the present study, we revise the IPS-derived SW speed data and normalize them to OMNI. We upgrade the algorithm to search the model parameters in calculating the smooth latitudinal SW speed profiles. We also upgrade the derivation of the SW density latitudinal structure.

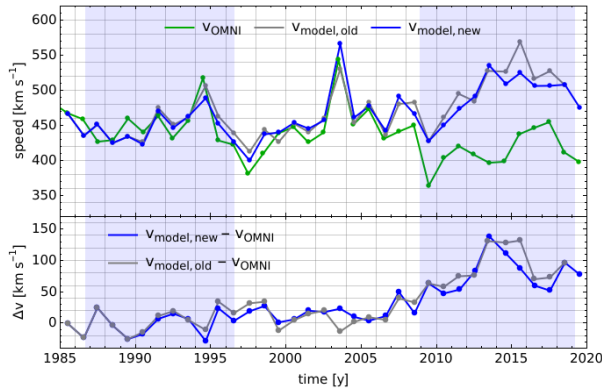


Figure 2: SW speed in the ecliptic plane at 1 au yearly averaged. We compare the time series for OMNI (v_{OMNI} ; dark green) with the model results before ($v_{\text{model, old}}$; gray) and after ($v_{\text{model, new}}$; blue)

updates described in Section 3.1.

3.1 Speed

We reconstruct the SW speed latitudinal variations in time and heliographic latitude following the method developed by Sokół et al. (2013). We use the most up-to-date SW speed data derived with the use of the computer-assisted tomography (CAT) method from the IPS observations from 1985 to 2019 (Kojima and Kakinuma 1991; Tokumaru 2013). We remove CRs with a small total number of points per a Carrington map (in practice, these are maps with significant observational gaps). We fit analytic functions to yearly averaged latitudinal profiles (Equation 3 in Sokół et al. (2013)). We upgrade the algorithm to determine the boundaries between the smooth-function components to reproduce the latitudinal profile. We search the boundaries automatically over the full set of possibilities now, and we select as final the set, which gives the smallest mean difference between the fitted smooth-function and the data. The effect of the upgrade of the fitting algorithm presents the comparison of the gray line ($v_{\text{model, old}}$) with the blue line ($v_{\text{model, new}}$) for years before 2011 in the top panel of Figure 2. The change for the ecliptic plane bin is mostly less than 5%. We present the upgraded model parameters to reproduce the smooth latitudinal profiles of the SW speed in Appendix A. We organize the model data in 10° -heliolatitudinal bins, with the 0° bin replaced with the CR-averaged OMNI measurements. The $\pm 10^\circ$ bins are linear interpolation of the 0° and the $\pm 20^\circ$ bins. We replace the $\pm 90^\circ$ bins by the value calculated from parabola fit to $\pm 70^\circ$ and $\pm 80^\circ$ bins. The resulting data set has a 10° resolution in heliolatitude and is based on yearly averaged IPS-derived SW speeds linearly interpolated to CRs.

Figure 2 presents a comparison of the yearly averages of the SW speed from the OMNI data (v_{OMNI} , dark green line) and the IPS-based model results (v_{model}) for the ecliptic plane. The difference in speed between these two data sets is, on average, about 16 km s^{-1} from 1985 to 2009 and about 85 km s^{-1} from 2011 to 2019 (bottom panel of Figure 2). The difference began to increase after 2007, remaining below 50 km s^{-1} , which is considered as an approximate uncertainty of the SW speed reconstructions from IPS observations. However, it

continued to increase from 2010 to 2015 and was greater than 100 km s^{-1} , in 2013 and 2014. The divergence of the IPS-derived SW speed from the OMNI data coincides in time with a few events. First, the *Ulysses* mission terminated in 2009 and is not available to cross-calibrate the SW latitudinal structure by independent, in-situ measurements. Second, the upgrade of the ISEE IPS multi-station facility in 2010. Third, the overall decrease in SW density, which decreased and next slightly recovered in the studied period as discussed in Section 2 (see also Figure 1). The in-ecliptic SW speed was, on average, $\sim 50 \text{ km s}^{-1}$ slower from 2009 to 2015 than from 1985 to 2009. After 2015, the average in-ecliptic SW speed recovered to about 440 km s^{-1} and decreased again after 2017 onward.

We revised IPS-derived SW speed data after 2010. Although new IPS sources were added to the IPS observations owing to the upgrade of the ISEE IPS system in 2010, the number of obtained IPS data reduced as compared to those before the system upgrade. The cause of this reduction is not fully understood yet, and it may be partly due to the weakening of IPS strength by a drop of the SW density fluctuations. We examined the effect of the reduced number of IPS data on the CAT analysis by comparing it with OMNI data. We found that the reduction does not significantly affect results of the CAT analysis, and also found that the CAT analysis yields a slightly better agreement with in situ measurements when it uses a larger angular width for blending lines-of-sight and a higher speed for an initial value of the iteration. We use the CAT analysis with the optimal settings to derived the SW speed distribution. Next, we use the revised data in the construction of the yearly latitudinal profiles from 2011 onward. We present the model results in blue in Figure 2. A comparison with the gray line, which illustrates the model results before the IPS-data revision, shows a reduction of the SW speed from 2014 to 2017. However, the SW speed remains higher than 500 km s^{-1} , while OMNI being about 420 km s^{-1} , for the period from 2011 to 2019.

A careful investigation of the IPS-derived SW speed suggests that the increase in speed observed in the ecliptic plane may be seen at all latitudes. We assume that the difference is a constant factor independent of latitude. We calculate the yearly

averages of the SW speed in the ecliptic plane from OMNI and the IPS-based model, determine the differences in speed, Δv , and reduce the yearly heliolatitudinal profiles of the model by Δv from 2011 to 2019, each year separately. The bottom panel in Figure 2 presents the Δv (the portion of the blue line starting from 2011). The Δv -adjustment reduces the speed out of the ecliptic plane during solar maximum and satisfies the agreement with in-situ measurements in the ecliptic plane. For 2010, when the IPS-derived SW speed data are not available, we calculate the heliolatitude profile as an average of the profile in 2009 and the revised profile in 2011. The difference between the model results and OMNI remains for 2009 and 2010 and has the same magnitude as the differences that happened before 2010. Thus there is no clear indication to revise the data up to 2010. We construct the final SW speed model results with the updated OMNI data in the ecliptic plane and the revised IPS-derived data adjusted to OMNI.

The IPS-derived SW speed data we use does not provide the accuracy of the SW speed derivation. Thus, we calculate the mean relative error of the model to the data to estimate the model uncertainty; it is about 8%. Additionally, we calculate the mean standard deviation of the data, which we used to calculate the yearly profiles to give a sense of the data variability. It varies from 70 km s^{-1} to 120 km s^{-1} , with the smaller (higher) value at higher (lower) latitudes.

We organize the model data into five heliolatitudinal bands ($<-90^\circ, -50^\circ>$, $<-40^\circ, -20^\circ>$, $<-10^\circ, 10^\circ>$, $<20^\circ, 40^\circ>$, $<50^\circ, 90^\circ>$) and present variations in time in these bands for the new model (color lines) and the old model (gray lines) in Figure 3. The most affected are data after 2010; it is because of the revision of the IPS-derived component of the model. The changes are the greatest for the SW out of the ecliptic plane, and for the slow SW speed during the solar maximum, less affected is the fast SW during solar minimum, it is less than 10%. The new SW speed is $\sim 25\%$ slower in the northern hemisphere and the mid-southern latitudes compared to the previous model during the solar maximum of SC 24. In the southern polar latitudes, the new model SW speed is $\sim 10\%$ slower. The changes for SCs 22 and 23 are less

than 5% and are due to the upgrade of the model algorithms.

The high latitude bands indicate SW speed variation typical for the SC variations, the high-speed streams during solar minimum, and the slow wind streams during solar maximum. These variations persist at mid-latitudes and fade out in the equatorial band. The periods of the presence of the slow SW at high latitudes differ in time in the North and the South hemispheres. We fit Gaussian functions to the SW speed variation in time in the polar bands ($<-90^\circ, -50^\circ>$, $<50^\circ, 90^\circ>$) for each SC separately and compare the full width at half maximum (FWHM) from the σ parameter ($\text{FWHM} = 2\sqrt{(2\ln 2)}/\sigma$) fitted to the data. We use the fitted FWHM as an indication of the length of the solar maximum period. The FWHM in years is 1.9 (2.3), 2.1 (3.9), and 4.4 (2.4) for SC 22, 23, and 24, in the North (South), respectively. The slow SW occupied the higher latitudes a few months longer in the South compared to the North in SC 22, and it remained almost twice as long in the South compared to the North in SC~23. The situation reversed in SC 24; the slow wind remained in the North almost twice as long as in the South. Moreover, the minimum SW speed in high-latitude bands decreased, which is a follow up of the decrease of the SW speed measured in the ecliptic plane (see Figure 1). The maximum SW speed value is similar in both hemispheres.

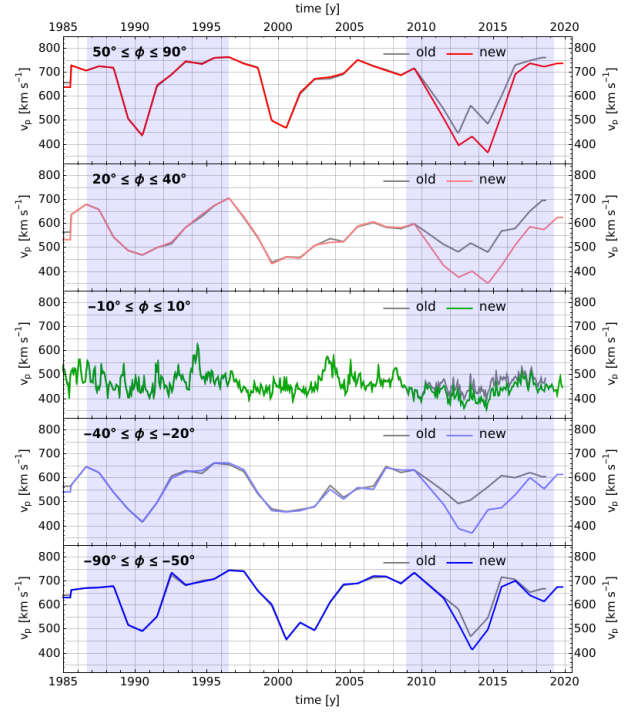


Figure 3: The model results for the SW speed variation in time. We averaged the data in heliolatitude in five bands indicated by the upper-left insets to each panel. The color lines illustrate the new model, and the gray lines present the old model. The shaded regions encompass SC 22 and 24.

3.2 Density

The IPS observations provide only the SW speed estimate. The SW density is the next parameter required to estimate the total ionization rates. The SW density is calculated from indirect measurements using several methods, e.g., Jackson & Hick (2004) used the Thomson scattering, Sokół et al. (2013) used the SW speed-density relation derived from *Ulysses* observations, and Sokół et al. (2015) used the empirical SW energy flux (le Chat et al. 2012). The SW energy flux is an empirical relation derived from *Ulysses* observations and is independent of latitude, similarly as the SW dynamic pressure (McComas et al. 2008).

In this study, we calculate the SW proton density variations in time and latitude (Equation 1a) based on the solar wind energy flux, W , calculated from the OMNI measurements (subscript “ecl” in

Equation 1b; see also Figure 1) smoothed in time over 13 CRs and the latitudinal variations of the SW speed derived in Section 3.1:

$$n_p(\phi, t) = 10^{-6} [m_p + (n_\alpha/n_p)(t) m_\alpha]^{-1} W(t) [v_p(\phi, t)(0.5v_{p,ecl}^2(\phi, t) + C)]^{-1}, \quad (1a)$$

$$W(t) = n_{p,ecl}(t)(m_p + (n_\alpha/n_p)_{ecl}(t) m_\alpha) v_{p,ecl}(t)(0.5v_{p,ecl}^2(t) + C), \quad (1b)$$

where t is time (in our study CRs), ϕ is the heliographic latitude, m_p is the proton mass, m_α is the mass of alpha particle, n_α/n_p is the alpha-to-proton abundance, W is the SW energy flux [$W \text{ m}^{-2}$], v_p is the SW speed [km s^{-1}], n_p is the SW density [cm^{-3}], and $C = GM_{\text{Sun}}R_{\text{Sun}}^{-1}$ where G is the gravity constant, M_{Sun} is the mass of the Sun, and R_{Sun} is the radius of the Sun. We apply the 13 CRs-moving average calculating W so as not to overestimate the short-scale in-ecliptic variations and do not propagate them to higher latitudes. As a result, we obtain SW proton density variations with CR resolution in time and 10° resolution in heliolatitude, as for the SW speed data from Section 3.1.

We organize the SW density model data into five heliolatitudinal bands, similarly, as for SW speed, and present the variations in time in Figure 4. The SW density is maximal at high latitudes during solar maximum and minimum during solar minimum. The variations in time show decrease at mid- and high-latitudes up to about 2010, and an increase afterward. These variations follow in time the decrease of the SW density observed in the ecliptic plane (see Figure 1). The new model shows SW density denser from about 2 to 4 cm^{-3} in the high latitudes during the solar maximum of SC 24 compared to the old model. The changes are the smallest in the southern polar region for which the SW density is denser less than 1 cm^{-3} . In the method we use, the SW density is derivative of the SW speed and thus follows the latitudinal asymmetries present in the SW speed. Comparing to Sokół et al. 2019a model, which used a different model, the SW density also changed for SCs 22 and 23. The higher SW density in the high latitudes during the solar maximum brings consequences for the study of the heliosphere, because the percentage increase in the SW density is greater than in the SW speed, and thus brings more in the charge exchange, see further discussion in Section 6.

According to the new model results, the North-South asymmetry of the SW density is greater in SCs~22 and 23 than in SC~24. In SCs 22 and 23, the SW density in the southern hemisphere has two peaks, while in the North hemisphere has only one peak which aligns in time with the first peak in the South. In SC 24, the SW was almost twice as dense in the North than in the South. We fit Gaussian functions to get an approximate estimate of the length of the period of enhanced density. The fitted FWHM is 1.95 (2.6), 1.63 (3.7), and 4.3 (3.0) in years for SC 22, 23, and 24, in the North (South), respectively. The numbers are comparable to the results of the same study for the SW speed because the SW density derives from the SW speed in the present model. The enhanced density persisted longer in the South hemisphere during SC~22 and 23; however, in SC~24, the SW was longer denser in the North than in the South.

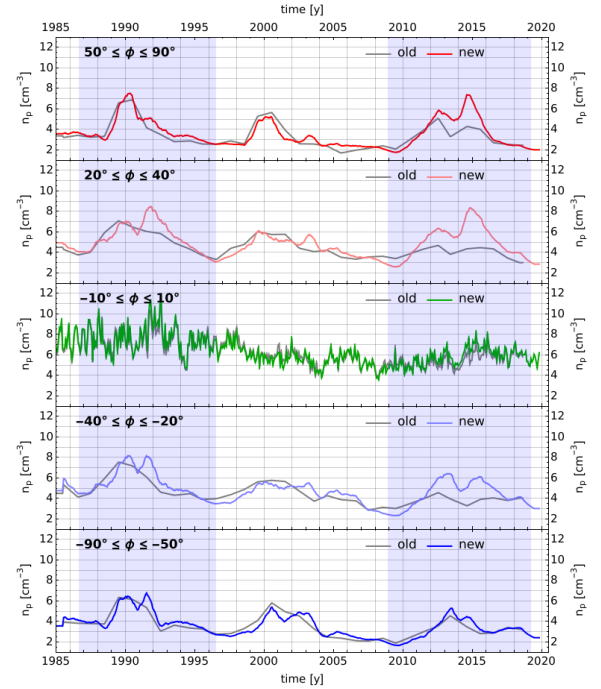


Figure 4: The model results for the SW density variation in time. We averaged the data in heliolatitude in five bands indicated by the upper-left insets to each panel. The color lines illustrate the new model, and the gray lines present the old model. The shaded regions encompass SC 22 and 24.

3.3 n_α/n_p

The n_α/n_p varies in time in the ecliptic plane, as discussed in Section 2, and as a function of latitude as measured by the Solar Wind Observations Over the Poles of the Sun (SWOOPS) onboard *Ulysses* (McComas et al. 2000, Ebert et al. 2009). *Ulysses* data also show that the n_α/n_p varies around an average of about 0.044 in latitudes higher than 40° (Figure 5, see also McComas et al. 2000). The alpha particles contribute to the charge exchange reaction for He, and the SW electron density ($n_e = n_p(1 + 2(n_\alpha/n_p))$) used, e.g., in the calculation of the electron impact ionization. However, these processes are of minor importance for the species discussed when compared to the charge exchange with the SW protons and photoionization reactions (see also Appendix B).

We include the variations of n_α/n_p in latitude based on *Ulysses* measurements out of the ecliptic plane and in time based on the OMNI measurements in the ecliptic plane. We fit Gaussian function ($g(\phi) = a \text{Exp}[-(\phi - b)^2/(2c^2)] + d$) to the n_α/n_p data measured by *Ulysses* during the first and third fast polar scans and determine the constant value of the n_α/n_p in high latitudes (parameter d) and the width of the low latitude band (parameter c) where the ratio diverges from the constant. These fitted parameters are $c = 11 \pm 1$ and $d = 0.0431 \pm 0.0008$. We present the fit in Figure 5. Next, we define the following Gaussian function to reproduce the heliolatitudinal profile of the n_α/n_p in time:

$$(n_\alpha/n_p)(t, \phi) = [(n_\alpha/n_p)_{\text{ecl}}(t) - 0.0431] \text{Exp}[-(\phi - \phi_{\text{Earth}}(t))^2/(2 \cdot 11^2)] + 0.0431 \quad (2)$$

where $(n_\alpha/n_p)_{\text{ecl}}(t)$ is the alpha-to-proton abundance measured in the ecliptic plane for the time t from OMNI data, $\phi_{\text{Earth}}(t)$ is the heliographic latitude of the Earth for the time t . This function guarantees the n_α/n_p as measured in the ecliptic and variable in time and the constant value in the higher latitudes as measured by *Ulysses* (a similar method was applied by Bzowski (2008) to reconstruct the SW speed and density variations in latitude). The Gaussian function approximates the transition from low to high latitudes and organizes the profile around the ecliptic plane and not the solar equator as the SW is. This bias the estimate of the n_α/n_p in this region; however, the data that we could use to study the temporal variation in this region are not available yet. Additionally, the

standard deviations of the hourly n_α/n_p data (see Section 2) is of a magnitude of the difference between the in-ecliptic and polar values. At last, using the n_α/n_p variable in time does not change the results significantly, for example, the in-ecliptic SW energy flux and dynamic pressure changes up to 10% compared to calculations with the n_α/n_p equal to 4% and mostly during the solar minimum and the solar maximum being much less in the intermediate phases of the solar activity. For the ionization reactions, the n_α/n_p contributes the most for He in the ecliptic plane at 1 au, the electron impact ionization changes up to ~5%, and the charge exchange reaction changes up to about 50%. However, the contribution of charge exchange reaction to the total ionization rates for He is smaller than 10%. For the remaining species, these effects are smaller than for He.

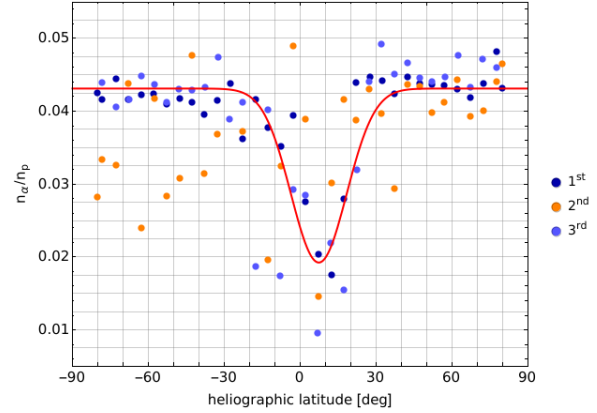


Figure 5: Helioatitudinal variation of the n_α/n_p measured by *Ulysses*/SWOOPS during the fast polar scans (color points). The Gaussian function fit to the data during the two solar minima is illustrated by the red line.

4. PHOTOIONIZATION

Photoionization by the solar EUV radiation is the next ionization process for heliospheric particles after the charge exchange reaction. The EUV spectrum in the wavelength range appropriate for calculation of the photoionization for the species observed by *IBEX* is provided by the Thermosphere Ionosphere Mesosphere Energetics and Dynamics (*TIMED*) mission via the Solar EUV Experiment (*SEE*) (Woods et al. 2005). The *TIMED*/*SEE* data are available from 2002 onward. An alternative data source of the EUV

spectrum for calculation of the photoionization rate would be the Solar Dynamics Observatory/EUV Variability Experiment (*SDO/EVE*) launched in 2010. However, due to a power anomaly in one of the instruments in 2014, the *SDO/EVE* data stopped being useful for photoionization rates studies. As a consequence, *TIMED/SEE* measurements remain the primary data source for calculation of the photoionization rates inside the heliosphere.

In the lack of appropriate observational data, the photoionization rates time series before the *TIMED/SEE* epoch should be calculated based on the solar activity indices. The most commonly used solar EUV proxies are the radio flux in 10.7 cm, F10.7 index (Tapping 2013), the Magnesium II core-to-wing index, $\text{MgII}_{c/w}$ (Heath & Schesinger 1986), the solar Lyman- α flux (Woods et al. 2000), and the integrated flux from the *SOHO/CELIAS/SEM* measurements (Judge et al. 1998). These were used in various combinations to calculate the photoionization rates for H, He, Ne, and O by, e.g., Bzowski et al. (2013a), Bochsler et al. (2014), Sokół & Bzowski (2014).

However, SC 24 brought several changes regarding the solar EUV proxy data. Wieman et al. (2014) reported calibration issues with the *SOHO/CELIAS/SEM* instrument, which measurements have been commonly used to estimate the photoionization rates, especially for He. Despite the calibration issues, the public *SOHO/CELIAS/SEM* data still present downward trends during the decreasing phase of SC 24, but the data improvements are no longer supported⁷. In the meantime, Snow et al. (2014) reported a change in the $\text{MgII}_{c/w}$ measured by instruments on the SOLar Radiation and Climate Experiment (*SORCE*; Rottman 2005) mission and suggested a change of data source for this quantity. Machol et al. (2020) reported improvements to the composite Lyman- α flux and change of the reference data for the composite series released by Laboratory for Atmospheric and Space Physics (LASP). The change of the Lyman- α flux has consequences for the study of the ISN H distribution inside the heliosphere because it changes the estimation of the radiation pressure, as discussed by Kowalska-Leszczynska et al. (2020). The ongoing calibration issues with the solar EUV proxies raise questions about the applicability of

these data for the estimation of the heliospheric photoionization rates, which should be as homogeneous between various species as possible to mitigate adverse, model-dependent effects. The only solar EUV proxy that seems to remain free from unresolved calibration issues and is released regularly is the F10.7 flux (Tapping 2013). In 2017, a new series of *TIMED/SEE* data were published (Version 12, Woods et al. 2018). The new, V12, measurements include a new EUV Grating Spectrograph (EGS) degradation trend based on rocket measurements and degradation trending analysis (Woods et al. 2018). The degradation analysis for *TIMED* V12 data is only through 2016, trending beyond are extrapolations and thus are less accurate⁸. The new version (V12) of *TIMED/SEE* data caused a change in the magnitude of the photoionization rates for ISN species calculated based on the previous data version (V11).

We use the *TIMED/SEE* data up to 2016.5 and the F10.7 index⁹ as a proxy of the photoionization rates for years when *TIMED/SEE* data are not available. Sokół & Bzowski (2014) proposed a method for reconstruction of the photoionization rates based on *TIMED/SEE* and F10.7 data, and we follow it here. We calculate the photoionization rates for H, He, Ne, and O by the integration of the *TIMED/SEE/Level3/V12* spectral data and applying the cross-sections from Verner et al. (1996). Next, we determine the relationship between the *TIMED*-derived photoionization rates and the F10.7 flux organizing the data into sectors and using the CR-averages as the reference time resolution.

The resulting relations are the following:

$$\beta_{\text{ph,H}} = -2.9819 \cdot 10^{-8} + 2.416 \cdot 10^{-8} f_{\text{F10.7}}^{0.4017} \quad \text{for H} \quad (3a)$$

$$\beta_{\text{ph,He}} = -2.8953 \cdot 10^{-8} + 4.4657 \cdot 10^{-9} f_{\text{F10.7}}^{0.7003} \quad \text{for He} \quad (3b)$$

$$\beta_{\text{ph,O}} = -1.991 \cdot 10^{-7} + 6.2847 \cdot 10^{-8} f_{\text{F10.7}}^{0.4836} \quad \text{for O} \quad (3c)$$

$$\beta_{\text{ph,Ne}} = -1.3585 \cdot 10^{-7} + 1.9731 \cdot 10^{-8} f_{\text{F10.7}}^{0.6538} \quad \text{for Ne} \quad (3d)$$

⁸ Source:

http://lasp.colorado.edu/data/timed_see/SEE_v12_release_notes.txt

⁹ Source: Natural Resources Canada, <https://spaceweather.gc.ca/solarflux/sx-5-en.php>

⁷ Leonid Didkovsky, February 2019, private communication

With the F10.7 data, we can reconstruct the photoionization rates from the late 1940s. Figure 6 presents the calculated photoionization rates and compares them with the previously used models (see, e.g., Sokół et al. (2019a)). The bottom portions of each panel illustrate the ratio of the new-to-old models. The change of the model due to the upgrade of the *TIMED/SEE* data affected rates for H, O, and Ne up to 35% with the new rates systematically higher than before. The new-to-old ratios for Ne and O increase with time during the ascending phase of SC 24, decrease after solar maximum, and next again increase in time. The least affected are the photoionization rates for He, up to almost 10% during the solar maximum period of SC 24. The trend of the changes for He is interesting because during solar minimum the new rates are higher, while during solar maximum, the new rates are smaller.

Additionally, as we present in the bottom portions of the panels of Figure 6, the ratios of the new to old models group into three periods: (1) from 2002 onward, related with the new version of *TIMED/SEE* data, (2) from about the 1970s to 2002, when the old model was composed with several EUV proxies, (3) from the 1940s to the 1970s, when the correlation with F10.7 in the old model was different due to the different version of the reference *TIMED/SEE* data.

The radial dependence of photoionization rates in the model follows r^{-2} . For the variations with heliographic latitude, we follow the relation from Equation 3.4 in Bzowski et al. 2013a (see also discussion in Sokół et al. (2019a)). The latitudinal anisotropy varies with distance to the Sun and is estimated to be $\sim 15\%$ at 1 au for chromospheric Lyman- α flux during solar minimum (Pryor et al. 1992, Auchère 2005). Additionally, the latitudinal variation may be different for different spectral lines (Kiselman et al. 2011). However, the topic of latitudinal variations of the photoionization rates is beyond the scope of this paper and is left for further studies. Here we only focus on the change of the magnitude of the in-ecliptic photoionization rates due to the change of the solar EUV data. The primary resolution in time is CR; however, we calculate the photoionization rates for daily time series for the *TIMED/SEE* data period only. We do not calculate the daily series for periods when we use the EUV proxies since the correlation changes (see, e.g., Bochsler et al. 2014).

The *TIMED/SEE/Level3/V12* data contain two estimates of the propagated relative uncertainties, the total accuracy, and the measurement precision. They both vary with wavelength and time. The mean total accuracy of in the period studied is 25% for wavelengths smaller than 26.5 nm, from 57% to 15% in the range from 27.5 to 33.5 nm, and $\sim 12\%$ for wavelengths up to 70 nm. The measurement precision is $\sim 3\%$ up to 26.5 nm and $\sim 32\%$ up to 70 nm. Tapping (2013) discusses the uncertainty of the F10.7 data, which are accurate to one solar flux unit (sfu) or 1% of the flux value, whichever is the larger. Additionally, the variability of the daily F10.7 data used to calculate the CR averages changes with the solar activity. The standard deviation is less than 1 sfu during solar minimum and greater than 30 sfu during solar maximum. The mean relative error of the photoionization rates calculated from the data to those reproduced by the model is 2% for H and 3% for He, Ne, and O; however, the goodness of the fit varies slightly in time and can be as much as 10% for H, and about 15% for He, Ne, and O.

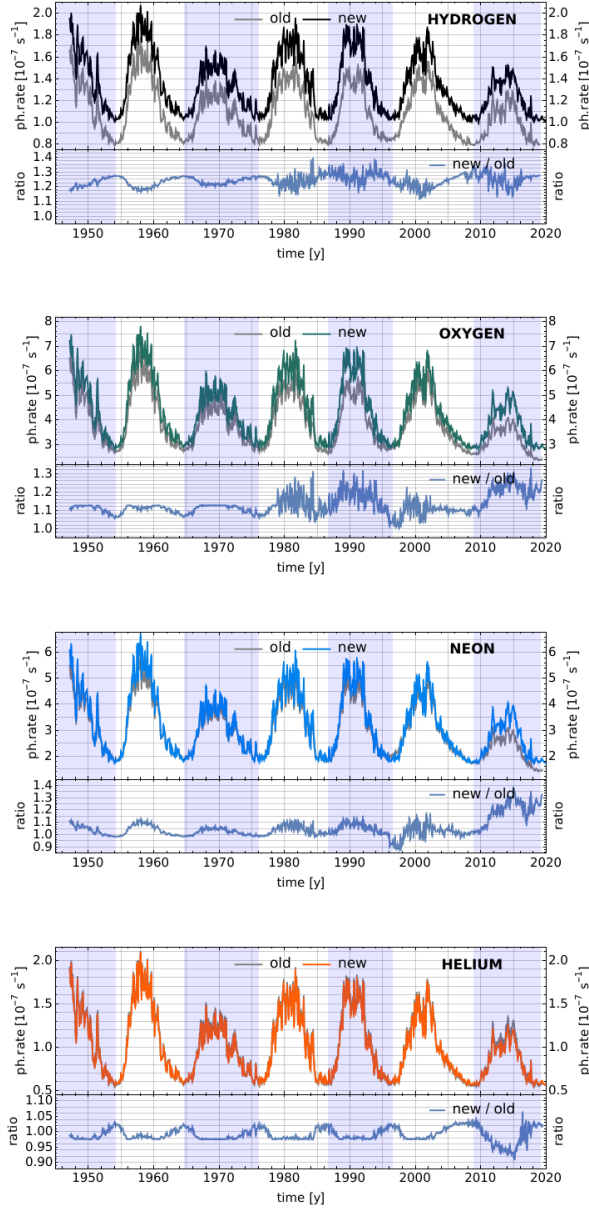


Figure 6: Photoionization rates for H, O, Ne, and He (from top to bottom) in the ecliptic plane at 1 au, CR-averaged in time, the new model (color line) compared with the old model (black line). Bottom portions of each panel provide a ratio of the new to the old rates. The shaded regions encompass the even SCs.

5. THE FINAL MODEL

With the in-situ measurements of the SW in the ecliptic plane (OMNI data), indirect observations of the SW speed latitudinal structure by the IPS observations, the direct measurements of the solar EUV irradiance measurements, and the measurements of the solar EUV proxies, we can construct a model of the ionization rates for heliospheric particles which is observation-based, continuous in time, and homogeneous among the species. This model follows the methodology developed by Sokół et al. (2013, 2015) for the SW latitudinal variations and Bzowski et al. (2013a,b) and Sokół & Bzowski (2014) for the composite model for calculation of the photoionization rates. This model constructs a complete system for calculating the Sun-Heliosphere Observation-based Ionization Rates (SHOIR).

The updates of the SW and solar EUV data change the most the estimation of the charge exchange and photoionization processes. The third ionization process, ionization by impact with the SW electrons, is the least affected. Calculating electron impact ionization, we follow the approach proposed by Ruciński & Fahr (1989, 1991) and Bzowski et al. (2008); however, we estimate the SW electron density accounting for the variations in time and latitude of the SW protons and n_{α}/n_p . As in Sokół et al. (2019a), we calculate the electron impact ionization using the relations only for the slow SW regime from Bzowski et al. (2008, 2013a), which is a first-order approximation. However, we apply it in the current calculations because the electron impact ionization contributes relatively minor to the total ionization rates at distances greater than 1 au. Nevertheless, a more thorough study of the electron impact ionization with latitude is needed for future studies.

The SHOIR model allows for reconstruction of the in-ecliptic variations of the charge exchange and electron impact ionization rates from the 1970s; the in-ecliptic variations of the photoionization rates from the late 1940s; the latitudinal variations of the total ionization rates (sum of charge exchange, photoionization, and electron impact ionization processes) starting from 1985 onward. In the present version, the latitudinal variations of the photoionization rates and the electron impact ionization rates are simplified and require further studies. However, the simplifications currently made are enough for the study of *IBEX* measurements

collected in the ecliptic plane. Also, reconstruction of the heliolatitudinal variations of the SW speed and density before 1985 is the aim of the future studies, since presently, in lack of available data, we use a constant profile averaged from data starting from 1985 onward. The radial dependence of the model includes an r^{-2} decrease of the SW density and photoionization, we assume that the SW speed is invariable with distance to the Sun, and the electron impact ionization follows the empirical radial dependence as discussed in Bzowski (2008). The baseline time resolution is the CR, and the resolution in latitude is 10° . The resolution in time can be increased to daily time series when limited to the ecliptic plane at 1 au and depends on data availability from OMNI and *TIMED*. Currently, SHOIR model allows to calculate ionization rates for H, He, Ne, and O. The model uses the most up-to-date solar source data, and thus appropriately accounts for the solar modulation of the ionization rates. The data sources used are regularly revised and the model components are adjusted to the data available to track the solar modulation as accurately as possible.

Figure 7 illustrates the variations of the SW speed and density in heliolatitude at 1 au for the last three SCs. The model reproduces the change of the high latitude SW from fast and dense during solar minimum to slow and less dense during solar maximum. It also follows the North-South asymmetry during the maximum of the solar activity (Tokumaru et al. 2015). The variation with latitudes of the slow SW flow closely follows the computed tilt angle of the Heliospheric Current Sheet (HCS) from the Wilcox Solar Observatory over time. The HCS model provides a radial boundary condition at the photosphere without polar field correction¹⁰ and is presented in yearly averages in Figure 7. The HCS model upper boundary is set at 70° , and the tilt angle reaches the maximum value when the slow SW streams encompass all latitudes. The agreement between the SW latitudinal variations with HCS additionally validates the model results.

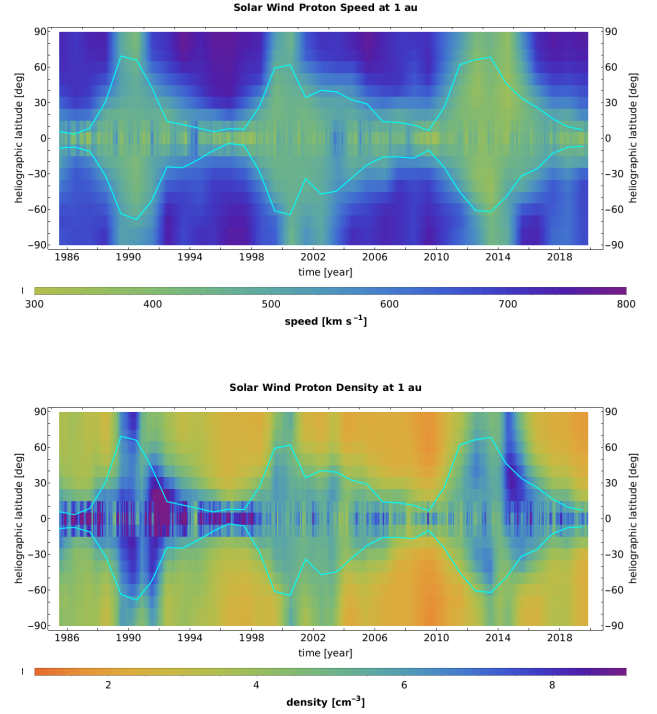


Figure 7: SW proton speed (top) and density (bottom) at 1 au calculated with the SHOIR model for the last three SCs (22-24). We overlay the yearly averages of the computed HCS (light blue line) on the maps.

The total ionization rates for the last three SCs calculated with the new model, for the ecliptic plane, and in the North and South polar directions for all four species, are presented in Figures 8 and 9, respectively. For comparison, we present the previously used model (e.g., in Sokół et al. 2019a) in gray lines. We see an overall decreasing trend for all species. The polar ionization rates are, in general, smaller than the ecliptic ones, except during the solar maximum periods when they are very similar. An interesting relation between in-ecliptic and polar total ionization rates is for H (top panels of Figures 8 and 9). The polar rates are similar in magnitude to the in-ecliptic ones for as long as a few years, however, only in one of the hemispheres. The time range when the total ionization rates for H in both hemispheres are as high as the in-ecliptic rates is very short. For example, in SC 24, the total ionization rates for H in the North hemisphere follow the in-ecliptic ionization rates from

¹⁰ Source: <http://wso.stanford.edu/Tilts.html>

2013 to 2015, while in the South, they are as high as the in-ecliptic ones for only 2-3 CRs. In contrast, for O, the total ionization rates in the North and South hemispheres are very similar, and thus the time range when they both are equal to the in-ecliptic rates is similar in length. For H, this behavior is due to the dominance of the charge exchange reaction in the total ionization rates, and thus the asymmetry in the SW structure propagates to the latitudinal structure of the total ionization rates. For O, the charge exchange and photoionization are comparably significant; however, a slightly greater contribution comes from photoionization, which is assumed symmetric in latitude in the model (see also discussion in Sokół et al. 2019a). For He and Ne, the differences between the polar and in-ecliptic total ionization rates are consequences of the approximate empirical latitudinal variation applied. Figure B1 in Appendix B illustrates the fractional contribution of individual ionization processes to the total ionization rates. We present the time-heliolatitude maps of the total ionization rates at 1 au for all four species discussed in Figure B2 in Appendix B.

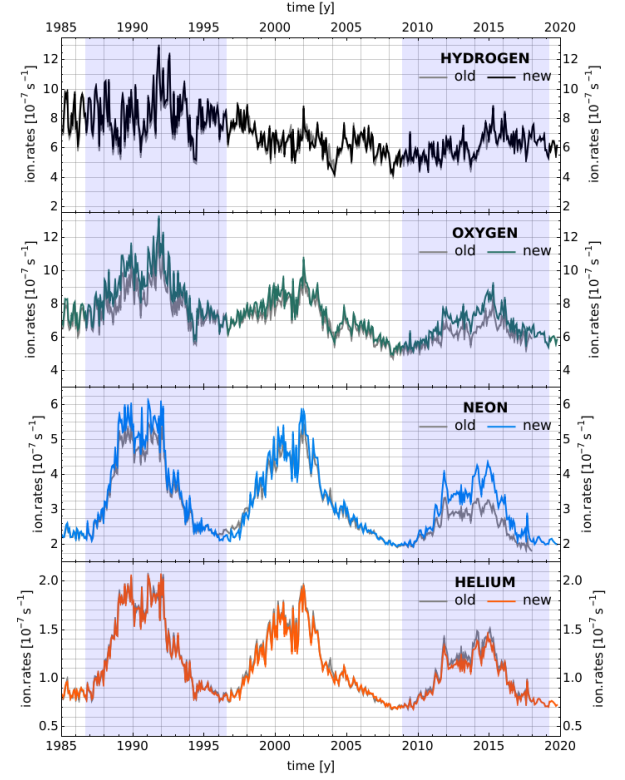


Figure 8: Total ionization rates for H, O, Ne, and He (from top to bottom) at 1 au in the ecliptic plane calculated with the new model (color lines) and the previous model (gray lines). The shaded regions encompass SC~22 and 24.

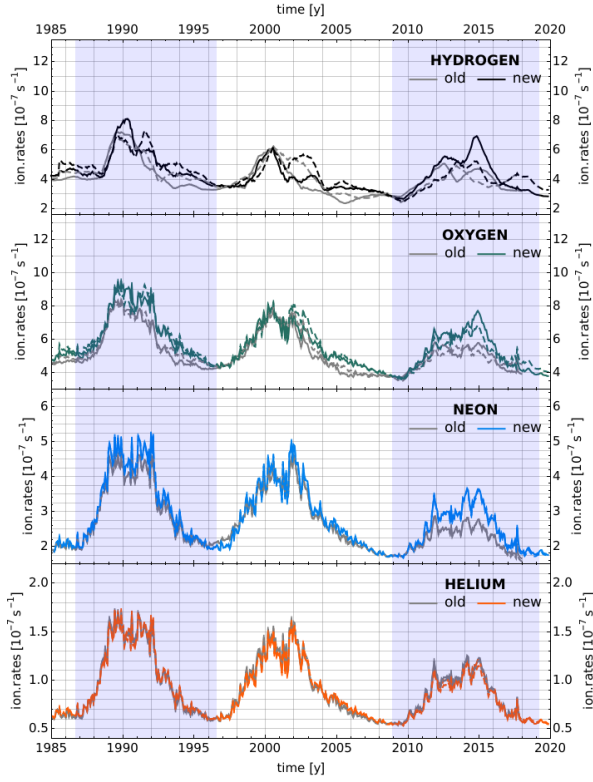


Figure 9: Same as Figure 8 but in the North (solid lines) and South (dashed lines) directions.

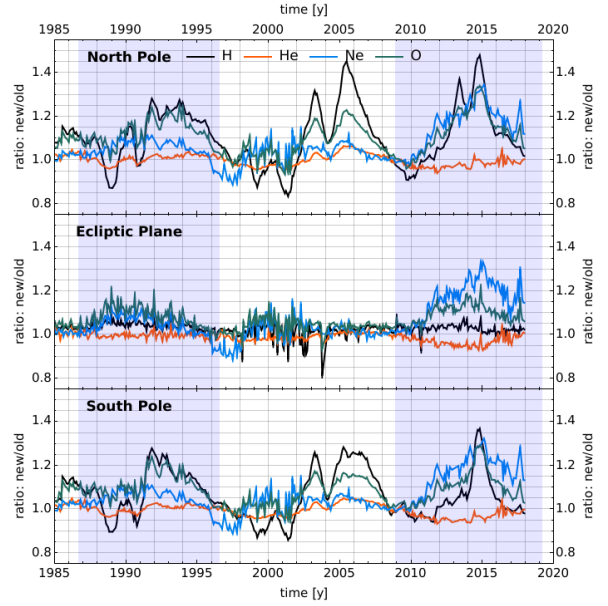


Figure 10: Ratios of the new to old models of the total ionization rates at 1 au presented in Figures 11 and 12.

6. DISCUSSION

The upgrade of the observation-based system for calculation of the ionization rates inside the heliosphere includes:

1. New release of the OMNI in-ecliptic SW data.
2. Revision of the SW speed latitudinal structure after 2010.
3. Adjustment of the IPS-derived SW speed to OMNI after 2010.
4. Modification of calculation of the latitudinal structure of the SW density.
5. A new model of the photoionization rates due to the upgrade of the *TIMED/SEE* data (Version 12).
6. Implementation of n_α/n_p variable in time in (a) the reconstruction of the latitudinal structure of the SW density, (b) the calculation of the SW electron density in the calculation of the electron impact ionization, and (c) the charge exchange with alpha particles for He.

The upgrade of the solar source data changed the heliospheric ionization rates in and out of the ecliptic plane. Figure 10 presents ratios of the new model to the old model at 1 au. The changes for the in-

ecliptic total ionization rates are less than 10% for H and He, up to 20% for O, and up to 35% for Ne. For H, O, and Ne the new total ionization rates are, in general, higher than the old ones. For He, the new in-ecliptic total ionization rates are smaller, especially during SC 24. The change of the source data was the greatest for the SC 24; thus, the changes in the total ionization rates are the greatest in this time range. The polar total ionization rates changed much more than the in-ecliptic ones. The most affected is H, for which the new polar ionization rates are up to 40% (30%) higher during solar maximum in 2015 in the North (South). The change is mostly due to the greater SW density calculated from the revised SW speed data. Interestingly, during the ascending phase of SCs 23, and for short time ranges in SCs 22 and 24, the polar total ionization rates for H are up to 15% smaller than in the previous model. The polar total ionization rates for O and Ne are higher up to 35% in the new model. However, the polar ionization rates for Ne and He are calculated by the approximate formula of the latitudinal scaling of the in-ecliptic values, and thus the in-ecliptic changes propagate to higher latitudes.

Summarizing, the upgrade of the source data affects the most the out-of-ecliptic total ionization rates for H and the least the total ionization rates for He. These bring consequences for the study of the heliosphere and the interstellar and heliospheric particles (ISN gas, PUIs, and ENAs), changing their fluxes, densities, and abundances. The change of the SW latitudinal structure also affects the interpretation of the spatial distribution of the full sky observations of the H backscatter radiation (the helioglow) in the Lyman- α line.

The higher ionization rates mean that the ISN gas and ENA fluxes are more strongly attenuated inside the heliosphere than previously thought. Thus, the fluxes in the source regions (in the heliosheath, in the VLISM) estimated based on the measurements at 1 au of these populations should be greater. The higher ionization rates affect the survival probability correction applied to the H ENA fluxes measured by *IBEX* (McComas et al. 2020, in preparation). The new survival probabilities are lower, which means that the measured H ENA flux is smaller compared to the flux at the boundary regions of the heliosphere (McComas et al. 2012, 2014, 2017). This change affects both the globally distributed flux (GDF) and the Ribbon (Schwadron et al. 2018). The ENA flux should

diminish stronger in the higher latitudes for time ranges corresponding to the solar maximum compared to the previous model. Additionally, the North-South asymmetry of the SW speed and density structure in latitude, and thus in the ionization rates, affects the latitudinal and energy dependence of the Ribbon. However, the general trends hold, and thus the general conclusions should remain unchanged (McComas et al. 2012, Swaczyna et al. 2016, Zirnstein et al. 2016, Dayeh et al. 2019). Additionally, the revision of the SW latitudinal structure with the slower and denser SW flow in the polar regions during the solar maximum of SC 24 can affect the estimation of the temporal variations of the dimension of the heliosphere from the study of the plasma pressure in the inner heliosheath (Reisenfeld et al. 2016). The higher ionization rates for H ENA fluxes and the slower and denser SW at high latitudes during solar maximum change the relationship between the H ENA fluxes in the source region observed in various epochs. This change will affect the study of the temporal and spatial variations of the spectral indices (e.g., Dayeh et al. 2012, Zirnstein et al. 2017, Desai et al. 2019a); however, quantitative assessment of the effects needs a separate study.

The higher ionization rates lead to the decrease of the density and flux of ISN gas species inside the heliosphere. The most significant effect should be observed in the downwind hemisphere, where part of the particles as on trajectories crossing the high latitudes before detection, especially for Ne and O for which the changes in the in-ecliptic total ionization rates are the greatest. The stronger attenuation of the ISN flux in the downwind hemisphere may affect the estimation of the ISN density in the downwind hemisphere, like ISN H density in the tail region of the heliosphere, which can be lower with the present model. Due to the changes in the magnitude and the latitudinal structure of the ionization rates, the variations of the ISN O density measured along the ecliptic plane should be more significant (see more in Sokół et al. 2019b). The change of the total ionization rates for various species changes the abundance ratios of these species inside the heliosphere and thus the determination of their abundances at the termination shock based on the measurements at 1 au. Also, the PUI production rates change with the change of the ISN gas density and the ionization rates. In general, the smaller the ISN gas

density close to the Sun, the smaller the interstellar PUIs density. Additionally, the more variable latitudinal structure of the ionization rates can result in a more significant variation of the inflow direction derived from the study of the PUI cone for the heavy species (Sokół et al. 2016). Quantitative assessment of the changes requires a separate study.

The solar modulation is an essential factor in the interpretation of the measurements and the studies of the heliosphere and its interaction with the VLISM. Fortunately, with available in-situ and remote measurements of the solar EUV and SW, we can follow the realistic solar modulation calculating the ionization rates. The observation-based source data are systematically improved, and thus while estimating the ionization rates, they should be regularly monitored and adjusted to the best current knowledge about the SW and the solar EUV flux available.

Acknowledgments. The OMNI data were obtained from the GSFC/SPDF OMNIWeb interface at <https://omniweb.gsfc.nasa.gov>.

The *TIMED/SEE/Level3/V012* data were obtained from the LASP http://lasp.colorado.edu/data/timed_see/level3/.

The solar radio flux F10.7 data were obtained from the Natural Resources Canada http://lasp.colorado.edu/data/timed_see/level3/.

The HCS computer tilt angles data were obtained from the WSO <http://wso.stanford.edu/>. The IPS observations were made under the solar wind program of the ISEE. JMS thanks Tom Woods and Don Woodraska for consultations regarding the *TIMED/SEE* data, and Leonid Didkovsky for consultations regarding the *SOHO/CELIAS/SEM* data. JMS acknowledges the research visit at ISEE, Nagoya University, Japan in February/March 2019 supported by the PSTEP program. JMS would like to thank Eric Zirnstein for helpful discussions regarding the manuscript. The study is funded by the Polish National Agency for Academic Exchange (NAWA) Bekker Program Fellowship PPN/BEK/2018/1/00049, the Polish National Science Center grant 2015/19/B/ST9/01328, and the *IBEX* mission as a part of the NASA Explorer Program (80NSSC18K0237).

Appendix A. Updated parameter tables from Sokół et al. 2013

The parameters of the SW structure model by Sokół et al. (2013) (their Tables 2 and 3) are updated by the presently used set of IPS-derived SW speed data and the upgraded algorithm to search for the best function to data fit. We present them in Tables 1 and 2.

Figure A1 illustrates the variation in time of the boundary parameters collected in Table 2. These parameters allow for reconstructing the yearly profiles of the smoothed SW speed structure in heliographic latitude. The SW speed profiles should be next normalized to OMNI in the ecliptic plane following the description in Section 3.1. Due to the lack of IPS-derived SW speed in 2010, we calculate the profile can as an average of the 2009 and 2011 profiles.

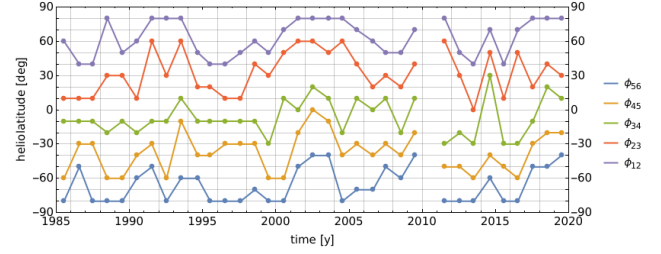


Figure A1: Variation in time of the boundary parameters given in Table 2.

Appendix B. Updates to Sokół et al. 2019a

Appendix B.1 Fractional contribution of individual ionization rates

Sokół et al. (2019a) presented in their Figure 3 variations in time of the fractional contribution of the individual ionization processes to the total ionization rates for H, O, Ne, and He in the ecliptic plane at 1 au. In Figure B1 we reproduce this figure for the upgraded ionization rates. The main changes are for the contribution from photoionization for H and O, which next slightly modified the relation between charge exchange and photoionization for total ionization rates for O, and change exchange estimate for He for which the contribution from charge exchange with α particles includes the n_α/n_p variable in time according to measurements.

Appendix B.2 Total ionization rate maps

Figure B2 presents time-heliolatitude maps of the total ionization rates at 1 au for H, O, Ne, and He. The time series to construct the maps have CR resolution in time and 10° resolution in latitude. The ionization rates for all species are the greatest in SC~22 and decrease onward.

Table 1. Update of Table 2 from Sokół et al. (2013)

Year	a_3	b_4	c_4	b_1	b_6	c_3
1985.53	466.075	-5.27944	-0.0225447	0.615288	2.74589	0.317373
1986.58	435.260	-22.6925	-0.383729	-0.362522	-0.54435	0.736723
1987.47	451.155	-14.6463	-0.205295	0.968966	0.543125	0.550488
1988.50	424.873	-7.48039	-0.0391982	-0.152901	-1.80871	0.140003
1989.52	434.126	-1.2069	0.00493784	-0.67455	1.63296	0.0626239
1990.51	422.892	-0.724207	-0.00562608	-1.94127	-3.50663	0.0481835
1991.53	470.051	-3.32495	-0.0665619	0.057286	-2.14836	0.0568465
1992.53	446.837	-6.42491	-0.0229758	0.39337	1.49494	0.167114
1993.53	429.901	-1.29765	0.324963	-0.0866007	0.51531	-0.00506922
1994.67	488.778	-9.64187	-0.111574	0.657815	-1.78586	0.283785
1995.52	452.042	-14.7493	-0.17597	0.605716	0.0565167	0.444155
1996.56	426.12	-20.9676	-0.304914	0.360896	-0.723424	0.770653
1997.59	399.859	-17.77	-0.227567	1.21111	-0.350789	0.623261
1998.57	437.176	-0.207988	0.105402	0.983069	0.0658812	0.11258
1999.53	439.881	5.52512	0.105683	2.49477	0.847357	0.00516689
2000.55	455.088	-0.083324	0.00214351	-1.7882	2.1444	0.0168461
2001.52	445.371	-2.10519	-0.0663024	-0.677565	-2.22267	0.0758078
2002.53	431.616	-1.15525	0.100776	0.505829	-0.288873	0.0369747
2003.61	597.871	-1.23323	-0.160777	-1.46248	-1.84231	0.155423
2004.55	461.288	3.508	0.128302	-0.284037	-1.44957	0.0512264
2005.53	471.241	0.81399	0.117815	1.00686	-0.687441	0.0600178
2006.64	441.985	-0.827241	0.0879785	0.141949	-0.0207413	0.262497
2007.51	518.460	-2.84317	0.0769017	-0.22037	0.0134445	0.354074
2008.55	465.760	-18.1012	-0.213819	1.57431	-0.0752352	0.209586
2009.48	391.003	0.523058	0.336663	-1.08514	-1.39841	-0.0276554
N/A	N/A	N/A	N/A	N/A	N/A	N/A
2011.54	473.761	2.34058	0.0929311	1.11697	3.70969	0.0364991
2012.58	491.613	7.46605	0.136153	1.6242	-0.994431	-0.0450805
2013.52	535.169	9.01221	0.112648	0.870457	1.50645	-0.0427767
2014.63	576.923	-1.99922	0.00978315	-0.260681	1.10823	0.085215
2015.57	524.688	12.7594	0.223909	2.8553	-0.474634	-0.0120651
2016.54	506.166	-4.81301	0.00374971	1.12025	-0.0484683	0.078162
2017.55	506.421	-5.0148	0.0238636	0.224164	1.07094	0.219366
2018.54	381.458	0.219091	0.216529	0.191434	0.159826	-0.0998319
2019.51	407.821	2.932	0.468517	0.828121	0.142181	-0.208931

NOTE—For 2010 the SW speed derived from IPS observation is not available. The latitudinal profile is calculate as an averaged of the 2009 and 2011 profiles.

Table 2. Update of Table 3 from Sokół et al. (2013)

Year	ϕ_{56} [°]	ϕ_{45} [°]	ϕ_{34} [°]	ϕ_{23} [°]	ϕ_{12} [°]
1985.53	-80	-60	-10	10	60
1986.58	-50	-30	-10	10	40
1987.47	-80	-30	-10	10	40
1988.5	-80	-60	-20	30	80
1989.52	-80	-60	-10	30	50
1990.51	-60	-40	-20	10	60
1991.53	-50	-30	-10	60	80
1992.53	-80	-60	-10	30	80
1993.53	-60	-10	10	60	80
1994.67	-60	-40	-10	20	50
1995.52	-80	-40	-10	20	40
1996.56	-80	-30	-10	10	40
1997.59	-80	-30	-10	10	50
1998.57	-70	-30	-10	40	60
1999.53	-80	-60	-30	30	50
2000.55	-80	-60	10	50	70
2001.52	-50	-20	0	60	80
2002.53	-40	0	20	60	80
2003.61	-40	-10	10	50	80
2004.55	-80	-40	-20	60	80
2005.53	-70	-30	10	40	70
2006.64	-70	-40	0	20	60
2007.51	-50	-30	10	30	50
2008.55	-60	-40	-20	20	50
2009.48	-40	-20	10	40	70
N/A	N/A	N/A	N/A	N/A	N/A
2011.54	-80	-50	-30	60	80
2012.58	-80	-50	-20	30	50
2013.52	-80	-60	-30	0	40
2014.63	-60	-40	30	50	70
2015.57	-80	-50	-30	10	40
2016.54	-80	-60	-30	50	70
2017.55	-50	-30	-10	20	80
2018.54	-50	-20	20	40	80
2019.51	-40	-20	10	30	80

NOTE—For 2010 see comment to Table 1.

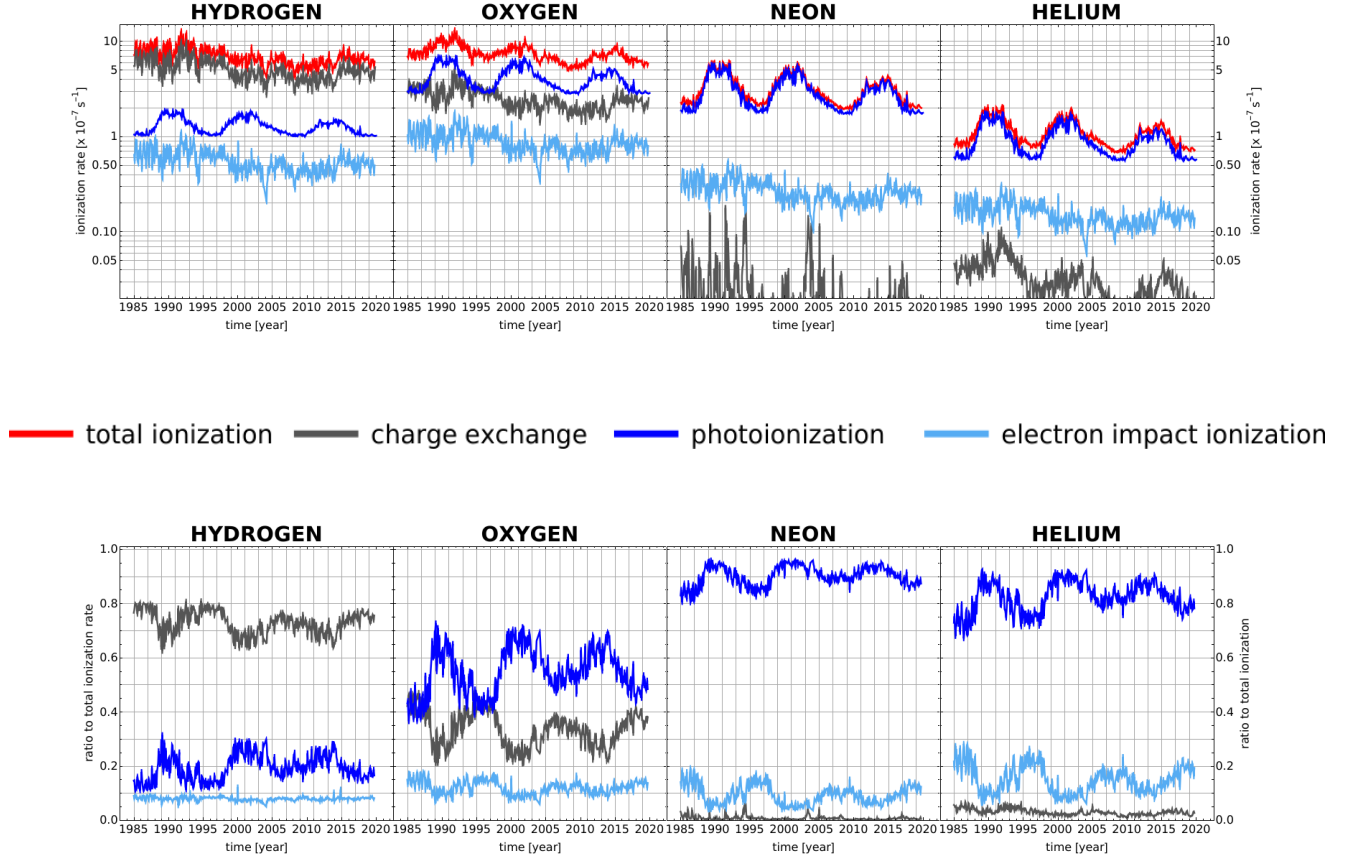


Figure B1: Top: time series of ionization rates due to various ionization processes for H, O, Ne, and He in the ecliptic plane at 1 au with CR resolution in time for the SC 24. Bottom: time series of the fraction of the individual ionization reaction rates to the total ionization rates for a given species. We present the color code between the two rows of panels.

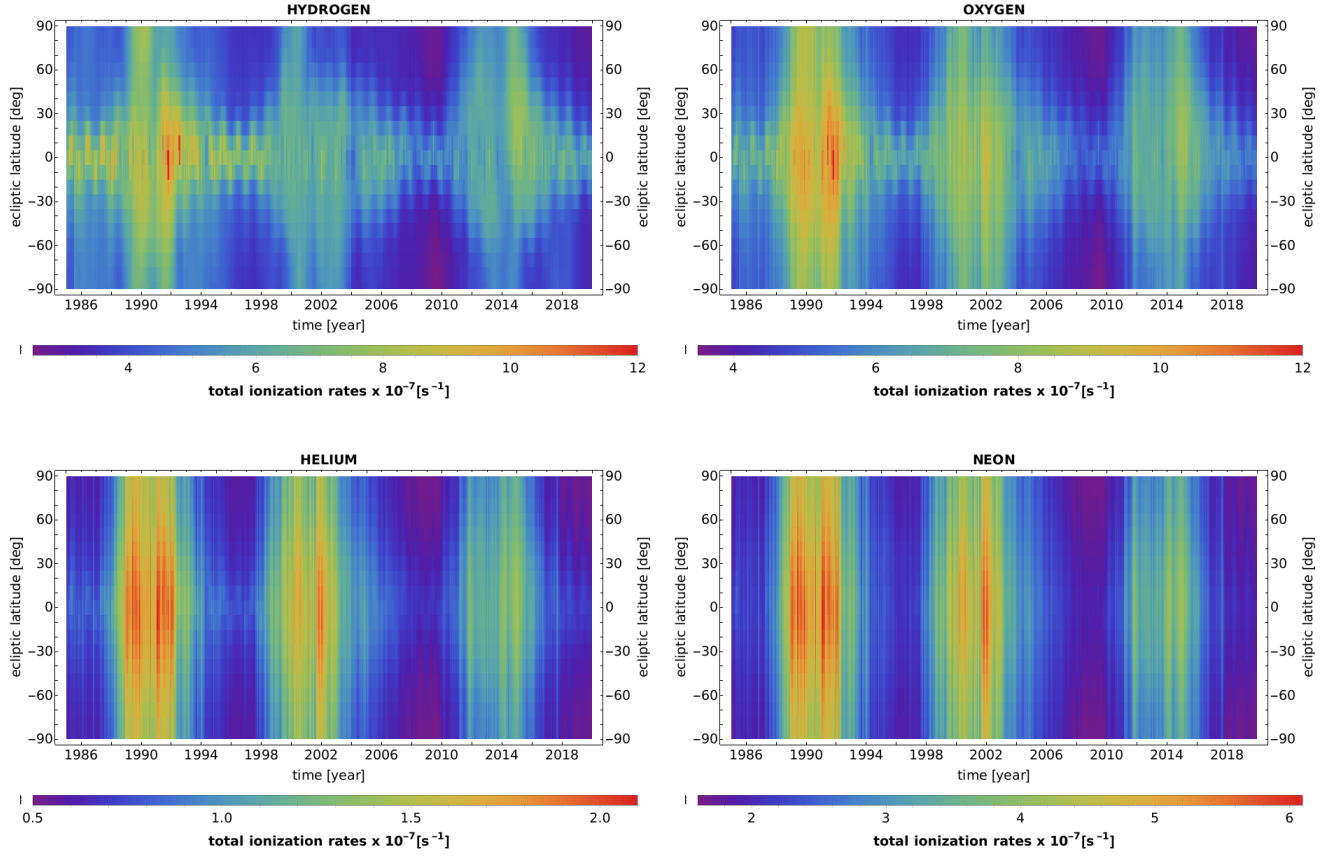


Figure B2: Maps of SHOIR calculated total ionization rates variations in time and ecliptic latitude at 1 au.

References

- Alterman, B. L., & Kasper, J. C. 2019, *ApJL*, 879, L6
- Auchère, F. 2005, *ApJ*, 622, 737
- Auchère, F., Cook, J. W., Newmark, J. S., et al. 2005a, *ApJ*, 625, 1036
- Auchère, F., Cook, J. W., Newmark, J. S., et al. 2005b, *Adv. Space Res.*, 35, 38
- Blum, P., & Fahr, H. J. 1970, *A&A*, 4, 280
- Bochsler, P., Kucharek, H., Möbius, E., et al. 472 2014, *ApJS*, 210, 12
- Bzowski, M. 2008, *A&A*, 488, 1057
- Bzowski, M., Mäkinen, T., Kyrölä, E., Summanen, T., & Quémérais, E. 2003, *A&A*, 408, 1165
- Bzowski, M., Möbius, E., Tarnopolski, S., Izmodenov, V., & Gloeckler, G. 2008, *A&A*, 491, 7
- Bzowski, M., Sokół, J. M., Kubiak, M. A., & Kucharek, H. 2013a, *A&A*, 557, A50
- Bzowski, M., Summanen, T., Ruciński, D., & Kyrölä, E. 2002, *J. Geophys. Res.*, 107, 10.1029/2001JA00141
- Bzowski, M., Kubiak, M. A., Möbius, E., et al. 2012, *ApJS*, 198, 12
- Bzowski, M., Sokół, J. M., Tokumaru, M., et al. 2013b, in *Cross-Calibration of Far UV Spectra of Solar Objects and the Heliosphere*, ed. E. Quémérais, M. Snow, & R. Bonnet, *ISSI Scientific Report No. 13* (Springer Science+Business Media), 67-138
- Coles, W. A., Rickett, B. J., Rumsey, V. H., et al. 1980, *Nature*, 286, 239
- Cook, J. W., Brueckner, G. E., & van Hoosier, M. E. 1980, *J. Geophys. Res.*, 85, 2257
- Cook, J. W., Meier, R. R., Brueckner, G. E., & van Hoosier, M. E. 1981, *A&A*, 97, 394
- Dayeh, M. A., McComas, D. J., Allegrini, F., et al. 2012, *ApJ*, 749, 50
- Dayeh, M. A., Zirnstein, E. J., Desai, M. I., et al. 2019, *ApJ*, 879, 84
- Dennison, P. A., & Hewish, A. 1967, *Nature*, 213, 343
- Desai, M. I., Dayeh, M. A., Allegrini, F., et al. 2019, *ApJ*, 875, 91
- Dudok de Wit, T. 2011, *A&A*, 533, A29
- Dudok de Wit, T., & Bruinsma, S. 2011, *Geophys. Res. Lett.*, 38, L19102
- Ebert, R. W., McComas, D. J., Elliott, H. A., Forsyth, R. J., & Gosling, J. T. 2009, *Journal of Geophysical Research (Space Physics)*, 114, A01109
- Heath, D. F., & Schlesinger, B. M. 1986, *J. Geophys. Res.*, 91, 8672
- Jackson, B. V., & Hick, P. P. 2004, in *Astrophysics and Space Science Library*, Vol. 314, *Astrophysics and Space Science Library*, ed. D. E. Gary & C. U. Keller, 355
- Judge, D. L., McMullin, D. R., Ogawa, H. S., et al. 1998, *SoPh*, 177, 161
- Kakinuma, T. 1977, in *Astrophysics and Space Science Library*, Vol. 71, *Study of Travelling Interplanetary Phenomena*, ed. M. A. Shea, D. F. Smart, & S. T. Wu, 101-118
- Kasper, J. C., Stevens, M. L., Lazarus, A. J., Steinberg, J. T., & Ogilvie, K. W. 2007, *ApJ*, 660, 901
- King, J. H., & Papitashvili, N. E. 2005, *J. Geophys. Res.*, 110, 2104
- Kiselman, D., Pereira, T., Gustafsson, B., et al. 2011, *A&A*, 535, A18
- Kojima, M., & Kakinuma, T. 1990, *Space Sci. Rev.*, 53, 173
- Kowalska-Leszczynska, I., Bzowski, M., Kubiak, M. A., & Sokół, J. M. 2020, *Update of the Solar Lyman- α Profile Line Model*, arXiv:2001.0706
- Le Chat, G., Issautier, K., & Meyer-Vernet, N. 2012, *SoPh*, 279, 197
- Machol, J., Snow, M., Woodraska, D., et al. 2020, *Earth and Space Science*, DOI:10.1029/2019EA000648
- McComas, D. J., Dayeh, M. A., Funsten, H. O., et al. 2019, *ApJ*, 872, 127
- McComas, D. J., Ebert, R. W., Elliot, H. A., et al. 2008, *Geophys. Res. Lett.*, 35, L18103
- McComas, D. J., Riley, P., Gosling, J. T., Balogh, A., & Forsyth, R. 1998a, *J. Geophys. Res.*, 103, 1955
- McComas, D. J., Bame, S. J., Barraclough, B. L., et al. 1998b, *Geophys. Res. Lett.*, 25, 1
- McComas, D. J., Barraclough, B. L., Funsten, H. O., et al. 2000, *J. Geophys. Res.*, 105, 10419
- McComas, D. J., Allegrini, F., Bochsler, P., et al. 2009, *SSRv*, 146, 11
- McComas, D. J., Dayeh, M. A., Allegrini, F., et al. 2012, *ApJS*, 203, 1
- McComas, D. J., Allegrini, F., Bzowski, M., et al. 2014, *ApJS*, 231, 28
- McComas, D. J., Zirnstein, E. J., Bzowski, M., et al. 2017, *ApJS*, 229, 41
- McComas, D. J., Dayeh, M. A., Funsten, H. O., et al. 2018, *ApJL*, 856, L10
- Pryor, W. R., Ajello, J. M., Barth, C. A., et al. 1992, *ApJ*, 394, 363
- Reisenfeld, D. B., Allegrini, F., Bzowski, M., et al. 2012, *ApJ*, 747, 110
- Reisenfeld, D. B., Bzowski, M., Funsten, H. O., et al. 2016, *ApJ*, 833, 277
- Reisenfeld, D. B., Bzowski, M., Funsten, H. O., et al. 2019, *ApJ*, 879, 1
- Rottman, G. 2005, *SoPh*, 230, 7
- Ruciński, D., Cummings, A. C., Gloeckler, G., et al. 1996, *SSRv*, 78, 73
- Ruciński, D., & Fahr, H. J. 1989, *A&A*, 224, 290
- Ruciński, D., & Fahr, H. J. 1991, *Ann. Geophys.*, 9, 102

- Schwadron, N. A., Allegrini, F., Bzowski, M., et al. 2018, ApJS, 239, 1
- Snow, M., Weber, M., Machol, J., Viereck, R., & Richard, E. 2014, Journal of Space Weather and Space Climate, 4, A04
- Sokół, J. M. 2016, Ph.D. thesis, Space Research Centre Polish Academy of Sciences (CBK PAN), Warsaw, Poland
- Sokół, J. M., & Bzowski, M. 2014, ArXiv e-prints, arXiv:1411.4826
- Sokół, J. M., Bzowski, M., & Tokumaru, M. 2017, in AGU Fall Meeting Abstracts, Vol. 2017, SH51D-2537
- Sokół, J. M., Bzowski, M., & Tokumaru, M. 2019a, ApJ, 872, 57
- Sokół, J. M., Bzowski, M., Tokumaru, M., Fujiki, K., & McComas, D. J. 2013, SoPh, 285, 167
- Sokół, J. M., Kubiak, M. A., & Bzowski, M. 2019b, ApJ, 879, 24
- Sokół, J. M., Swaczyna, P., Bzowski, M., & Tokumaru, M. 2015, SoPh, 290, 2589
- Swaczyna, P., Bzowski, M., & Sokół, J. M. 2016, ApJ, 827, 71
- Tapping, K. F. 2013, Space Weather, 11, 1
- Thomas, G. E. 1978, Ann. Rev. Earth Planet. Sci., 6, 173
- Tokumaru, M., 2013, Proceedings of the Japan Academy, Series B, 89, 67
- Tokumaru, M., Fujiki, K., & Iju, T. 2015, J. Geophys. Res., 120, 3283
- Tokumaru, M., Kojima, M., & Fujiki, K. 2010, J. Geophys. Res., 115, A04102
- Tokumaru, M., Kojima, M., & Fujiki, K. 2012, Journal of Geophysical Research (Space Physics), 117, 6108
- Tokumaru, M., Kojima, M., Fujiki, K., Maruyama, K., Maruyama, Y., Ito, H., & Iju, T., 2011, Radio Sci., 46, RS0F02
- Verner, D. A., Ferland, G. J., Korista, T. K., & Yakovlev, D. G. 1996, ApJ, 465, 487
- Wenzel, K.-P., Marsden, R. G., Page, D. E., & Smith, E. J. 1989, Advances in Space Research, 9, 25
- Wieman, S. R., Didkovsky, L. V., & Judge, D. L. 2014, SoPh, 289, 2907
- Woods, T. N., Eparvier, F. G., Harder, J., & Snow, M. 2018, SoPh, 293, 76
- Woods, T. N., Tobiska, W. K., Rottman, G. J., & Worden, J. R. 2000, J. Geophys. Res., 105, 27195
- Woods, T. N., Eparvier, F. G., Bailey, S. M., et al. 2005, J. Geophys. Res., 110, A01312
- Zirnstein, E. J., Dayeh, M. A., McComas, D. J., & Sokół, J. M. 2017, ApJ, 846, 63
- Zirnstein, E. J., Funsten, H. O., Heerikhuisen, J., & McComas, D. J. 2016, A&A, 586, A31
- Zirnstein, E. J., Heerikhuisen, J., McComas, D. J., et al. 2018, ApJ, 859, 104